Weyl points in photonic-crystal superlattices

Weyl points in photonic-crystal superlattices

Jorge Bravo-Abad,[1] Ling Lu,[2] Liang Fu,[2] Hrvoje Buljan,[3] and Marin Soljačić[2]

[1] *Departamento de Física Teórica de la Materia Condensada and Condensed Matter Physics Center (IFIMAC), Universidad Autónoma de Madrid, E-28049 Madrid, Spain*

[2] *Department of Physics, Massachusetts Institute of Technology, Cambridge, MA 02139 USA*

[3] *Department of Physics, University of Zagreb, Bijenička c. 32, 10000 Zagreb, Croatia*

Abstract

We show that Weyl points can be realized in all-dielectric superlattices based on three-dimensional layered photonic crystals. Our approach is based on creating an inversion-breaking array of weakly-coupled planar defects embedded in a periodic layered structure with a large omnidirectional photonic band gap. Using detailed band structure calculations and tight-binding theory arguments, we demonstrate that this class of layered systems can be tailored to display three-dimensional linear point degeneracies between two photonic bands, without breaking time-reversal symmetry and using a configuration that is readily-accessible experimentally. These results open new prospects for the observation of Weyl points in the near-infrared and optical regimes and for the application of Weyl-physics in integrated photonic devices.

Stimulated by the extraordinary properties of graphene [1–3], the development of artificial systems displaying Dirac-like physics has become a very active research area of condensed-matter science and related fields [4]. In this context, photonic-crystal structures [5] and photonic lattices (waveguides arrays) have emerged as versatile platforms for mimicking with light waves the electronic transport properties of graphene [6–30]. Specific examples of the exotic phenomena enabled by the presence of photonic Dirac cones include conical diffraction [6], pseudo-diffuse light transport [7], directional optical waveguiding [8, 9, 11], photonic Klein tunneling [14], angular selectivity of spontaneous emission [30], pseudo-magnetic properties in the optical regime [23] and large-area single-mode behavior [20, 27].

This endeavor for creating *photonic-graphene* systems has also inspired novel ways of accessing fundamental physical phenomena that, although originally predicted in the context of condensed-matter theory, are difficult (if not virtually impossible) to observe in electronic systems. A good example are Weyl points –the higher dimensional analogs of photonic Dirac points. Derived for the first time almost nine decades ago to describe massless chiral fermions [31], Weyl points feature unique topological properties from which rich new physics has been predicted to stem [32–44]. Remarkably, very recently, the first experimental observations of Weyl points have been reported in a three-dimensional double-gyroid photonic crystal [45] and in Fermi-arc surface states of TaAs [46, 47]. In this work, we report on a novel route to realize Weyl points in a layered photonic structure that is suitable for optical integration. First, we obtain line node dispersion by creating a periodic array of weakly-coupled planar defects embedded in a three-dimensional (3D) photonic crystal. Then, we break the inversion-symmetry of the system by varying the interlayer coupling between every three layers. Using detailed *ab-initio* electromagnetic (EM) calculations, we show that this class of systems exhibits Weyl points in their band structure.

A schematic view of the considered system is displayed in Fig. 1. The underlying 3D photonic-crystal structure (yellow volumes in Fig. 1) consists of an alternating stack of *rod layers*, formed by a triangular lattice of dielectric rods of index n_b, and *hole layers*, consisting of dielectric slabs (also of index n_b) milled by a triangular lattice of air holes. The radius and height of the dielectric rods are r_c and h_c, respectively, whereas the thickness of the dielectric slabs and the radius of the air holes are r_h and h_s, respectively. Both the rod and hole triangular lattices feature the same lattice constant a. The structure is also characterized by a sequential in-plane shift between consecutive layers. Specifically, the in-

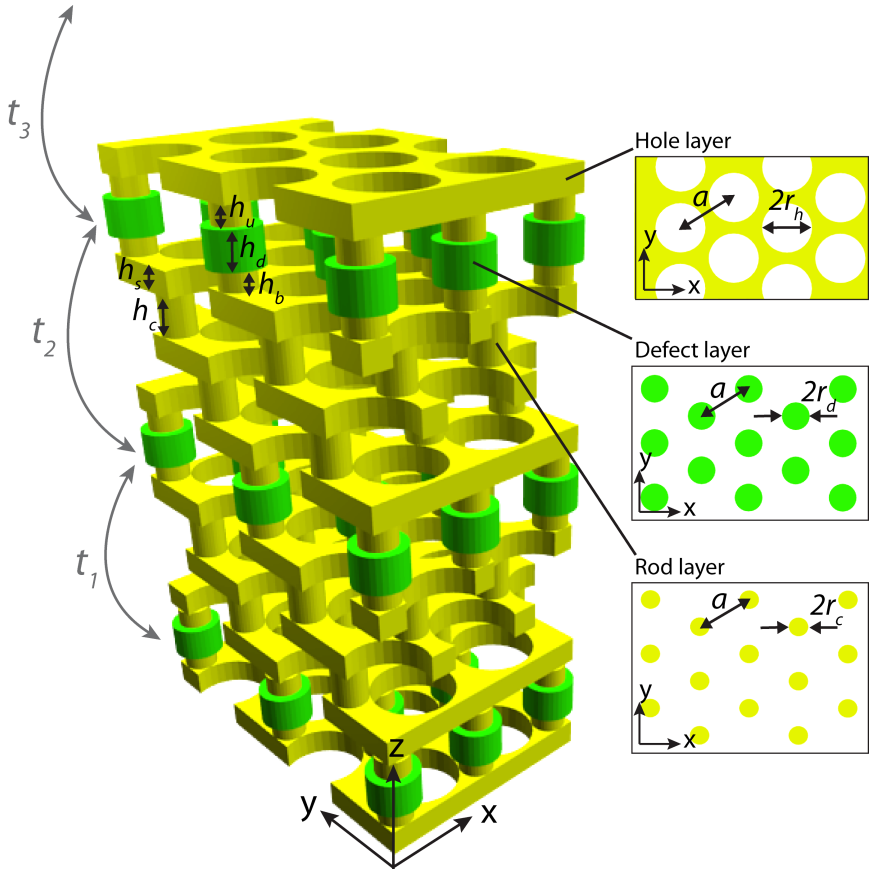

FIG. 1. Schematic view of the layered three-dimensional photonic crystal analyzed in this work. Transversal cross-sections of the rod, hole and defect layers are displayed in the right insets. The geometrical parameters defining each of the layers, as well as the reference system, are also included in the figure. The parameters t_1, t_2 and t_3 represent the electromagnetic coupling between the corresponding planar defects of the array.

plane triangular lattice of each of the layers is sequentially shifted following the positions of a ABC stacking, $\mathbf{r}_A = (0,0)$, $\mathbf{r}_B = a(1/(2\sqrt{3}), 1/2)$, $\mathbf{r}_C = a(1/\sqrt{3}, 0)$. Note that the unit cell in the out-of-plane direction (z-direction) consists of an alternating stack of 3 rod layers and 3 hole layers. This class of structures was proposed for the first time in Ref. [48] as the result of creating an fcc lattice of overlapping air cylinders in a dielectric medium. Its significance in photonics stems mainly from their large omnidirectional bandgap (usually larger than 20% for common integrated photonics materials), its suitability for optical device integration using a layer-by-layer approach [49], and its highly-controllable optical response through the individual modification of only one of the layers forming the structure [50, 51].

As shown in Fig. 1, in the analyzed structure, a one-dimensional array of planar defects is embedded inside the above described layered 3D photonic-crystal. These planar defects are introduced by replacing each of the rods forming the rod-layers lying at position A (within the ABC sequence mentioned before) by a three-cylinder column made from a defect rod of index n_d (green rods in Fig. 1) sandwiched by two short rods of index n_b. The defect rods have radius r_d and height h_d. The dielectric cylinders on top and bottom have heights h_u and h_b, respectively, and the same radius as the rods in the rod-layers (r_c). Notably, by changing the values of h_u and h_b separately, one can control the electromagnetic coupling between a given planar defect and its upper and lower nearest-neighbor planar defects (the couplings between three consecutive layers are represented by t_1, t_2, and t_3 in Fig. 1). In addition, in the realization sketched in Fig. 1, there are three hole-layers and two rod-layers separating nearest-neighbor planar defects. Placing the planar defects at closer distances to each other would make the EM coupling between nearest-neighbor defect planes to depart from the weak-coupling condition used in our approach.

We start by analyzing the properties of a configuration in which all planar defects forming the array have the same geometrical parameters (this case corresponds to make $t_1 = t_2 = t_3$ in Fig. 1). Figure 2 displays the corresponding band structure, obtained by assuming the following set of geometrical parameters: $r_c = 0.26a$, $h_c = 0.50a$, $r_h = 0.45a$, and $h_s = 0.32a$ (defining underlying 3D photonic crystal), and $r_d = 0.32a$, $h_d = 0.30a$, and $h_u = h_b = 0.24a$ (defining the defect planes). The refractive indices of the high-index regions of the system are $n_b = 3.5$ and $n_d = 4.0$. These values for n_b and n_d are assumed in all the calculations shown in this work. Yellow areas in Fig. 2 render the projected band structure for the perfectly periodic 3D photonic crystal (i.e., the photonic crystal without the defect layer). This dispersion diagram was obtained by plotting the frequencies ω of the extended bulk states of the system as a function of the in-plane wavevector along the high-symmetry directions of the Irreducible Brillouin Zone (IBZ) corresponding to a 3D hexagonal lattice (see inset of Fig. 2). Solid blue lines in Fig. 2 display the dispersion relation of modes associated to the array of planar defects. All the calculations displayed in this work have been performed with a supercell method using the MIT Photonic-Bands package [52].

As deduced from Fig. 2, the considered 3D photonic crystal exhibits a large omnidirectional band gap, centered at a frequency $\omega = 0.4550\,(2\pi c/a)$ (c is the speed of light in vacuum) and featuring a gap-midgap ratio of 19%. Of special interest among the number of

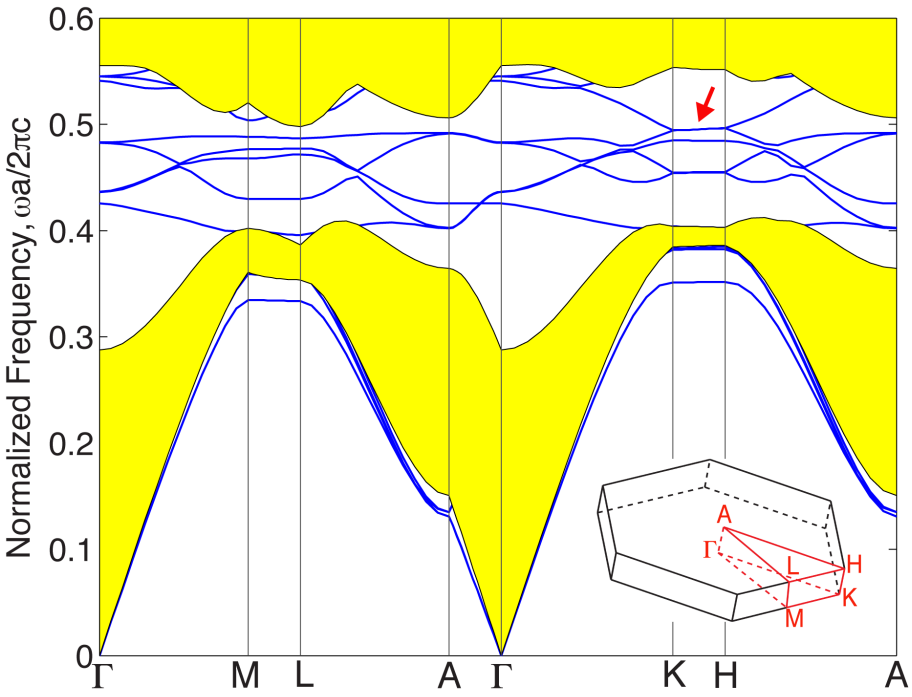

FIG. 2. Photonic band structure of the array of defect planes depicted in Fig. 1, as computed for a configuration featuring inversion symmetry (t_1=t_2=t_3). The following geometrical parameters have been assumed in the calculations: $r_c = 0.26a$, $h_c = 0.50a$, $r_h = 0.45a$, and $h_s = 0.32a$, $r_d = 0.32a$, $h_d = 0.30a$, and $h_u = h_b = 0.24a$ (see the definition of these parameters in Fig. 1). The refractive indices of the high-index regions of the system system are $n_b = 3.5$ and $n_d = 4.0$. Yellow areas display the bulk photonic bands of the system, whereas the blue solid lines correspond to the modes supported by the planar defects. The inset shows a sketch of the corresponding 3D hexagonal First Brilloun Zone, together with its corresponding high-symmetry points. The red arrow marks the position of the band corresponding to a line node.

defect bands that can be observed inside this full band gap is the frequency-isolated band centered at a frequency $\omega_D = 0.4951\,(2\pi c/a)$ that emerges along the K-H direction (marked by a red arrow in Fig. 2). An enlarged view of that band is displayed in Fig. 3(a) (see blue solid lines). The physical origin of this band can be understood by using the following tight-binding picture of this problem. When isolated in the underlying 3D photonic crystal, each of the planes forming the defect array exhibits a frequency-isolated Dirac cone in the (k_x, k_y) plane at the K-point [20]. The effective Hamiltonian close to that Dirac point can be expressed as $H_{2D}(k_x, k_y) = \hbar\omega_D + \nu_x k_x \sigma_x + \nu_y k_y \sigma_z$, where ν_i are the group velocities and

σ_i are the Pauli matrices. Diagonalization of $H_{2D}(k_x, k_y)$ yields the canonical Dirac-cone dispersion $\omega_{2D}(k_x, k_y) = \omega_D \pm \sqrt{\nu_x^2 k_x^2 + \nu_y^2 k_y^2}$. When extended to 3D, $H_{2D}(k_x, k_y)$ actually describes a line node, i.e., two bands that are forming a line degeneracy along k_z (as illustrated by the cyan solid lines in Fig. 3(a)), but that they disperse linearly along the other two directions [38, 39]. Now, to describe the array of planar defects considered in Fig. 2, we introduce an additional term (representing the coupling between nearest-neighbor planar defects) to the effective Hamiltonian, H_{2D}. This yields the following new Hamiltonian $H_{3D}(\mathbf{k}) = H_{2D}(k_x, k_y) - 2t\cos(k_z d)\mathbb{1}$ (where $\mathbf{k} = (k_x, k_y, k_z)$, d is the periodicity of the defect array along z and $\mathbb{1}$ is the unity matrix). Diagonalization of $H_{3D}(\mathbf{k})$ produces a dispersion relation given by $\omega_{3D}(\mathbf{k}) = \omega_{2D}(k_x, k_y) - 2\,t\cos(k_z\,d)$, which agrees in all three-dimensions with the dispersion obtained from our bands structure calculations (see green dots and inset of Fig. 3(a); the latter shows the Dirac cones obtained in the (k_x, k_y) plane for an exemplary k-point along K-H). Thus, from this analysis we can conclude that a line node (featuring cosine-like dispersion) emerges in the considered system as the result of periodically stacking weakly-coupled planar defects, each of which exhibits Dirac cones when isolated.

Next, in order to create Weyl points from this line node, it is crucial to consider the significant fundamental differences between Dirac points and Weyl points. Dirac cones are protected by *PT-symmetry*, which is the product of time-reversal symmetry (T) and parity (P) inversion (note that here we discuss PT-symmetry only in the context of Hermitian systems). Weyl points, on the other hand, are topologically protected gapless dispersions that can exist only when PT-symmetry is broken. This necessary condition for the realization of Weyl points can be deduced from the Hamiltonian that governs Weyl point dispersions, $H_W(\mathbf{k}) = \nu_x k_x \sigma_x + \nu_y k_y \sigma_y + \nu_z k_z \sigma_z$. Indeed, the term σ_y of $H_W(\mathbf{k})$ can exist only when PT-symmetry is broken [38, 39]. Thus, in order to realize Weyl points in the analyzed class of systems without breaking time-reversal symmetry, we need to break the inversion-symmetry ($\epsilon(\mathbf{r}) = \epsilon(-\mathbf{r})$, where $\epsilon(\mathbf{r})$ is the dielectric constant distribution) that the array of planar defects considered in Fig. 4(a) features with respect to the center of the defect rods. To do that, we introduce three different values (t_1, t_2, and t_3) of the EM coupling between the planar defects and their corresponding upper nearest-neighbor defect layers. More specifically, we create an inversion-symmetry breaking superlattice of defect layers formed by stacking periodically (following the configuration shown in Fig. 1) three different defect layers featuring three different values of the parameter h_u (see definition of that parameter in Fig.

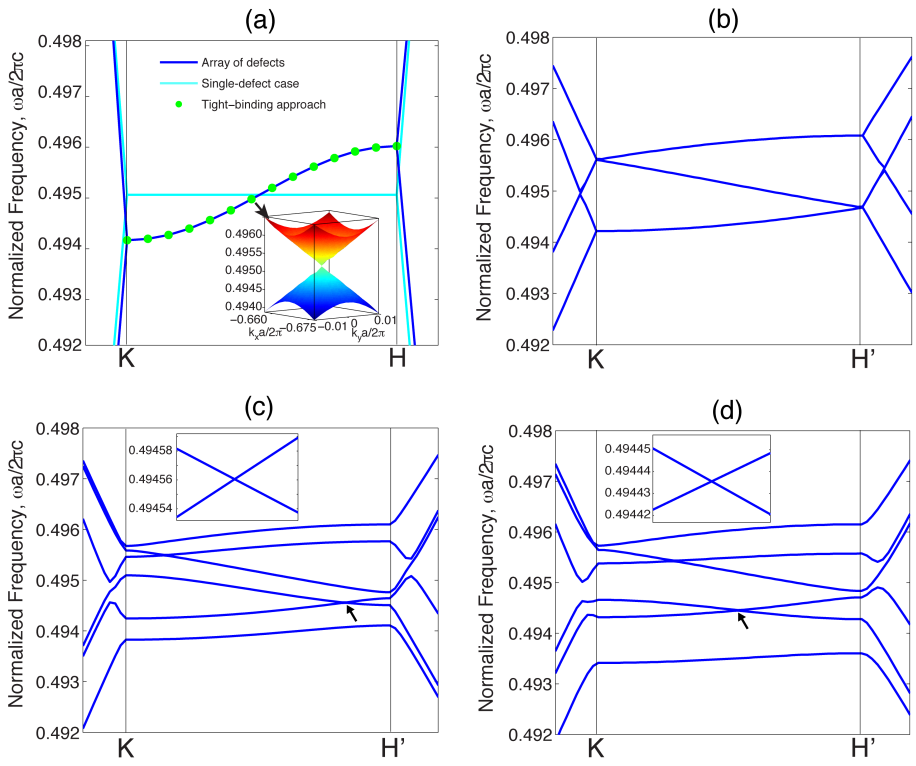

FIG. 3. (a) Enlarged view of the band marked with an arrow in Fig. 2 (blue solid lines). For comparison, the results corresponding to the single-defect configuration are also displayed (cyan solid lines). Green dots correspond to the analytical tight-binding expression discussed in the main text. The inset shows the Dirac cones obtained at the indicated point of the K-H path. (b) Computed band structure of the system considered in (a), but now calculated with an artificial supercell three times larger along z. (c) Photonic band structure of the array of defects depicted in Fig. 1, as computed for a configuration with broken inversion symmetry (with different values of the interlayer couplings t_1, t_2 and t_3). The considered superlattice of defect layers is formed by periodically stacking three planar defects featuring the following sequence of values for the parameter h_u/a: 0.245, 0.250, and 0.255. (d) Same as (c), but now with a sequence of h_u/a values given by 0.240, 0.250, and 0.260. The insets of both panels render an enlarged view of the band crossing marked by an arrow in the corresponding main panel.

1). By varying h_u, we modify the degree of overlap between the evanescent-field tails of two nearest-neighbor defect layers, and consequently the mutual EM coupling between them.

The first important point to realize regarding the superlattice described above is that its

unit cell along z is three times larger than of the array discussed in Fig. 3(a). The larger unit cell leads to a *folding* of the photonic bands along k_z (the high-symmetry path of the IBZ along k_z is now three times smaller, which yields a new limit, H', of the IBZ along k_z). To illustrate this point, Fig. 3(b) displays the folded bands of the same structure considered in Fig. 3(a) (which still retains inversion symmetry), but now computed using an artificial supercell of size $3d$ along the z direction. Note that, as can be deduced from tight-binding arguments, the considered three-defect unit cell (featuring three different couplings t_1, t_2 and t_3) is the minimal system that breaks PT-symmetry in this structure. A system featuring only two different couplings (t_1 and t_2) always presents inversion symmetry.

The second important point to highlight derives from the symmetry arguments discussed above. Based on the fact that Dirac cones are not robust to PT-symmetry breaking, we expect that the degeneration between the two bands forming each of the superlattice folded bands (shown in Fig. 3(b)) is lifted once the inversion symmetry is broken (i.e., once the three different interlayer couplings t_1, t_2 and t_3 are introduced into the system). This is apparent from the band structures rendered in Figs. 3(c) and 3(d), which correspond, respectively, to two superlattices with increasing asymmetry. Figure 3(c) corresponds to the following sequence of h_u/a values of the three defect layers forming the unit cell: 0.240, 0.245, and 0.255. Figure 3(d) corresponds to the following sequence of h_u/a values: 0.240, 0.250, and 0.260. The rest of geometrical parameters are the same as those used for Fig. 2. As seen, the frequency difference between the originally degenerated bands increases as the asymmetry in the system grows. Remarkably, these results show clearly how the combination of the bands folding and the degeneracy lift induced by the asymmetry enables the type of band crossings needed for the realization of Weyl points. Insets of Figs. 3(c) and (d) show enlarged views of the band crossings found for both configurations at $\omega \approx 0.4945(2\pi c/a)$ (the examined crossings are marked with arrows in their corresponding main panels). As observed, linear dispersion is obtained near the two considered band crossings (similar linear dispersions were obtained for the other crossings that can be observed in Figs. 3(c) and 3(d) at $\omega \approx 0.4955(2\pi c/a)$), which represents a clear signature of the emergence of Weyl points in this class of systems.

There are four Weyl points in the considered structure, with their *Chern numbers* (taking values $+1$ or -1) cancelling each other in pairs (the Chern number of a Weyl point is defined as the integral –within the 3D Brillouin zone of the structure– of the Berry curvature on a

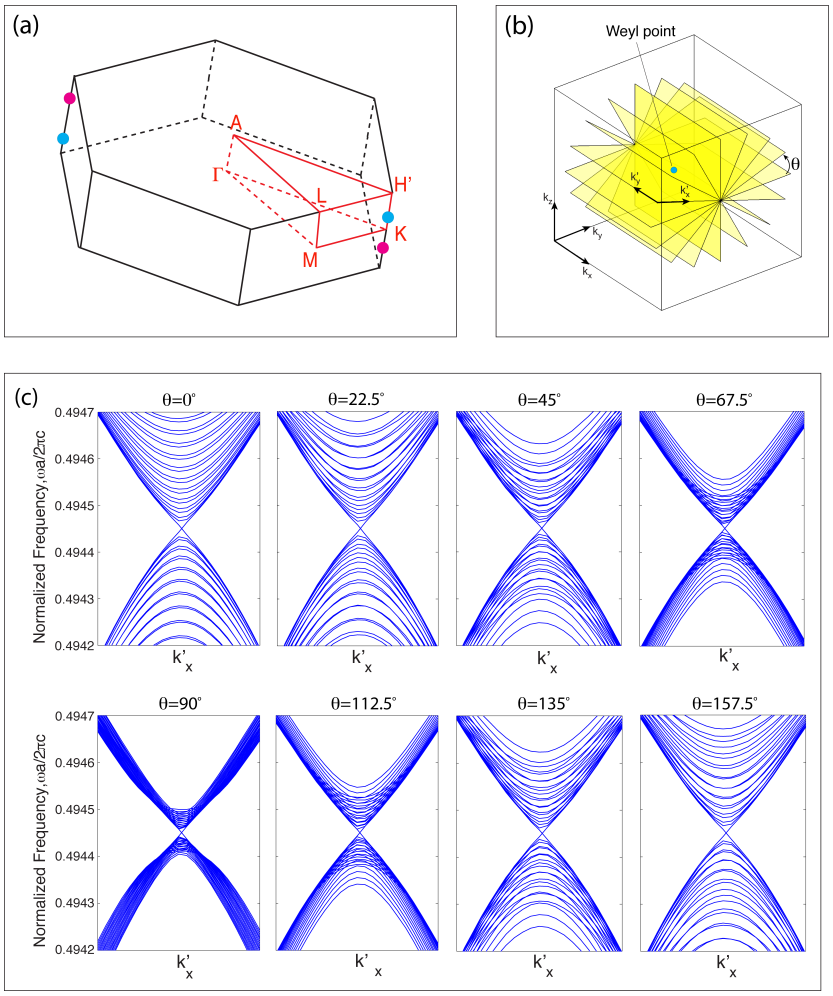

FIG. 4. (a) Illustration of the location in the First Brillouin Zone of the four Weyl points displayed by the analyzed structure. Blue and pink circles represent Weyl points with opposite Chern numbers. (b) Sketch of the different orientations of the k-space planes considered in (c). The definition of the rotation angle θ, as well as the intrinsic in-plane reference system of each plane, (k'_x, k'_y), are displayed. The location of the considered Weyl point is also indicated. (c) Computed projected bands along k'_x corresponding to eight planes that sample θ in the interval $[0, 2\pi)$, as shown in (b).

closed surface enclosing the considered Weyl point [39]). In addition to the two Weyl points discussed above, there is another pair of Weyl points with opposite chirality. Time-reversal symmetry maps a Weyl point at $\mathbf{k}$ to $-\mathbf{k}$, without changing its Chern number. Then, the presence in the structure of a mirror symmetry plane along z (which crosses the xy-plane along y=0, see definition of axes in Fig. 1), maps these Weyl points to two Weyl points with opposite Chern numbers. Thus, from these symmetry arguments, it derives that the

analyzed system displays a total of four Weyl points at the boundaries of the First Brillouin Zone (see schematic illustration in Fig. 4(a)). This is the minimal number of Weyl points possible without breaking time-reversal symmetry [38].

Finally, to check numerically that the dispersion relation of the analyzed structure is linear in three-dimensions around the observed band crossings, we have carried out extensive numerical calculations of the projected bands over a large number of planes with different orientations in k-space. Figure 4(c) summarizes the results obtained for the band crossing displayed in inset of Fig. 3(d) (similar results were obtained for the other band crossings described above). The orientation of each k-space plane is defined by the rotation angle θ defined in Fig. 4(b). Specifically, Fig. 4(c) displays the results corresponding to eight values of θ that sample the interval $[0, 2\pi)$. Similar calculations were performed for the same set of angles but replacing the rotation axis by the k_y and k_z axes. In all considered cases the projected bands along the intrinsic k_x axis of each of the rotated planes (labeled as k'_x in Fig. 4(b)) exhibit a linear degeneration point at the band crossing, which demonstrates that the degeneration point observed in inset of Fig. 3(d) is indeed a Weyl point.

The proposed class of systems could be experimentally realized in the near-field frequency region using a lithographic layer-by-layer approach [49]. Hydrogenated amorphous silicon (a-Si:H) and a Silicon-Germanium alloy (such as Si_xGe_{1-x} with x=0.25) could be used for fabricating the underlying photonic crystal and the defect layers, respectively (the refractive indexes of these materials at λ=1.55μm are similar to the ones employed in our numerical calculations [53, 54]). On the other hand, it could be also possible to experimentally realize the proposed class of systems in the microwave region using an approach similar to the one described in Ref. [45]. Further optimization of the geometrical parameters of the structure and the refractive indexes will be required in order to increase the bandwidth of the Weyl dispersion analyzed in this work.

In conclusion, we have presented a novel approach to realize Weyl points in all-dielectric and integrable layered photonic systems. We expect our results will stimulate further research on the experimental observation of Weyl points in the visible and near-infrared regimes, with applications in nano-scale coherent light generation, quantum information processing, and solar energy harvesting. The analyzed class of systems also offers a versatile platform for the discovery and demonstration of novel phenomena in the emerging field of topological photonics. Furthermore, the approach introduced in this work can be ex-

tended to obtaining Weyl points in condensed-matter systems by stacking two-dimensional materials such as graphene and BN [55].

This work was supported in part by the U.S. Army Research Laboratory and the U.S. Army Research Office through the Institute for Soldier Nanotechnologies, under contract number W911NF-13-D-0001. L.L. and M.S. were supported in part by the Solid-State Solar-Thermal Energy Conversion Center (S3TEC), an Energy Frontier Research Center funded by the U.S. Department of Energy, Office of Science, Office of Basic Energy Sciences under Award Number DE-SC0001299. L.L. was supported in part by the MRSEC Program of the National Science Foundation under award number DMR-1419807. H.B. and M.S. acknowledge support from the Unity through Knowledge Fund, Grant 5/13.

[1] A. K. Geim and K. S. Novoselov, "The rise of graphene," Nat. Mat. **6**, 183–191 (2007).

[2] A. H. Castro Neto, F. Guinea, N. M. R. Peres, K. S. Novoselov, and A. K. Geim, "The electronic properties of graphene," Rev. Mod. Phys. **81**, 109–162 (2009).

[3] F. Bonaccorso, Z. Sun, T. Hasan, and A. C. Ferrari, "Graphene photonics and optoelectronics," Nat. Photonics **4**, 611–622 (2010).

[4] M. Polini, F. Guinea, M. Lewenstein, H. C. Manoharan, and V. Pellegrini, "Artificial honeycomb lattices for electrons, atoms and photons," Nat. Nanotech. **8**, 625–633 (2013).

[5] J. D. Joannopoulos, S. G. Johnson, J. N. Winn, and R. D. Meade, *Photonic crystals: Molding the flow of light, 2nd Ed.* (Princeton Univ. Press, 2008).

[6] O. Peleg, G. Bartal, B. Freedman, O. Manela, M. Segev, and D. N. Christodoulides, "Conical diffraction and gap solitons in honeycomb photonic lattices," Phys. Rev. Lett. **98**, 103901 (2007).

[7] R. A. Sepkhanov, Ya. B. Bazaliy, and C. W. J. Beenakker, "Extremal transmission at the Dirac point of a photonic band structure," Phys. Rev. A **75**, 063813 (2007).

[8] F. D. M. Haldane and S. Raghu, "Possible realization of directional optical waveguides in photonic crystals with broken time-reversal symmetry," Phys. Rev. Lett. **100**, 013904 (2008).

[9] Z. Wang, Y. D. Chong, J. D. Joannopoulos, and M. Soljacic, "Reflection-free one-way edge modes in a gyromagnetic photonic crystal," Phys. Rev. Lett. **100**, 013905 (2008).

[10] X. Zhang, "Observing Zitterbewegung for photons near the Dirac point of a two-dimensional

photonic crystal," Phys. Rev. Lett. **100**, 113903 (2008).

[11] Z. Wang, Y. Chong, J. D. Joannopoulos, and M. Soljacic, "Observation of unidirectional backscattering-immune topological electromagnetic states," Nature **461**, 772–775 (2009).

[12] M. J. Ablowitz, Sean D. Nixon, and Y. Zhu, "Conical diffraction in honeycomb lattices," Phys. Rev. A **79**, 053830 (2009).

[13] T. Ochiai and M. Onoda, "Photonic analog of graphene model and its extension: Dirac cone, symmetry, and edge states," Phys. Rev. B **80**, 155103 (2009).

[14] O. Bahat-Treidel, O. Peleg, N. Grobman, M.and Shapira, M. Segev, and T. Pereg-Barnea, "Klein tunneling in deformed honeycomb lattices," Phys. Rev. Lett. **104**, 063901 (2010).

[15] U. Kuhl, S. Barkhofen, T. Tudorovskiy, H.-J. Stöckmann, T. Hossain, L. de Forges de Parny, and F. Mortessagne, "Dirac point and edge states in a microwave realization of tight-binding graphene-like structures," Phys. Rev. B **82**, 094308 (2010).

[16] S. R. Zandbergen and M. J. A. de Dood, "Experimental observation of strong edge effects on the pseudodiffusive transport of light in photonic graphene," Phys. Rev. Lett. **104**, 043903 (2010).

[17] O. Bahat-Treidel and M. Segev, "Nonlinear wave dynamics in honeycomb lattices," Phys. Rev. A **84**, 021802 (2011).

[18] A. Szameit, M. C. Rechtsman, O. Bahat-Treidel, and M. Segev, "$\mathcal{PT}$-symmetry in honeycomb photonic lattices," Phys. Rev. A **84**, 021806 (2011).

[19] X. Huang, Y. Lai, Z. H. Hang, H. Zheng, and C. T. Chan, "Dirac cones induced by accidental degeneracy in photonic crystals and zero-refractive-index materials," Nat. Mat. **10**, 582–586 (2011).

[20] J. Bravo-Abad, J. D. Joannopoulos, and M. Soljacic, "Enabling single-mode behavior over large areas with photonic Dirac cones," Proc. Nat. Acad. Sci. USA **109**, 9761–9765 (2012).

[21] D. Jukic, H. Buljan, D.-H. Lee, J. D. Joannopoulos, and M. Soljacic, "Flat photonic surface bands pinned between Dirac points," Opt. Lett. **37**, 5262–5264 (2012).

[22] S. Bittner, B. Dietz, M. Miski-Oglu, and A. Richter, "Extremal transmission through a microwave photonic crystal and the observation of edge states in a rectangular Dirac billiard," Phys. Rev. B **85**, 064301 (2012).

[23] M. C. Rechtsman, J. M. Zeuner, A. Tunnermann, S. Nolte, and A. Segev, M.and Szameit, "Strain-induced pseudomagnetic field and photonic Landau levels in dielectric structures,"

Nat. Photonics **7**, 153–158 (2013).

[24] M. C. Rechtsman, Y. Plotnik, J. M. Zeuner, D. Song, Z. Chen, A. Szameit, and M. Segev, "Topological creation and destruction of edge states in photonic graphene," Phys. Rev. Lett. **111**, 103901 (2013).

[25] M. Bellec, U. Kuhl, G. Montambaux, and F. Mortessagne, "Topological transition of Dirac points in a microwave experiment," Phys. Rev. Lett. **110**, 033902 (2013).

[26] G. Weick, C. Woollacott, W. L. Barnes, O. Hess, and E. Mariani, "Dirac-like plasmons in honeycomb lattices of metallic nanoparticles," Phys. Rev. Lett. **110**, 106801 (2013).

[27] S.-L. Chua, L. Lu, J. Bravo-Abad, J. D. Joannopoulos, and M. Soljacic, "Larger-area single-mode photonic crystal surface-emitting lasers enabled by an accidental Dirac point," Opt. Lett. **39**, 2072 (2014).

[28] K. Xie, H. Jiang, A. D. Boardman, Y. Liu, Z. Wu, M. Xie, P. Jiang, Q. Xu, M. Yu, and L. E. Davis, "Trapped photons at a Dirac point: a new horizon for photonic crystals," Laser Phot. Rev. **8**, 583–589 (2014).

[29] Y. Plotnik, M. C. Rechtsman, D. Song, M. Heinrich, J. M. Zeuner, S. Nolte, Y. Lumer, N. Malkova, J. Xu, A. Szameit, Z. Chen, and M. Segev, "Observation of unconventional edge states in photonic graphene," Nat. Mat. **13**, 57–62 (2014).

[30] P. Moitra, Y. Yang, Z. Anderson, I. I. Kravchenko, D. P. Briggs, and J. Valentine, "Realization of an all-dielectric zero-index optical metamaterial," Nat. Photonics **7**, 791–795 (2013).

[31] H. Weyl, "Elektron und gravitation," Z. Phys. **56**, 330–352 (1929).

[32] X. Wan, A. M. Turner, A. Vishwanath, and S.Y. Savrasov, "Topological semimetal and Fermi-arc surface states in the electronic structure of pyrochlore iridates," Phys. Rev. B **83**, 205101 (2011).

[33] A. A. Burkov and L. Balents, "Weyl semimetal in a topological insulator multilayer," Phys. Rev. Lett. **107**, 127205 (2011).

[34] G. Xu, H. Weng, Z. Wang, X. Dai, and Z. Fang, "Chern semimetal and the quantized anomalous hall effect in $HgCr_2Se_4$," Phys. Rev. Lett. **107**, 186806 (2011).

[35] P. Delplace, J. Li, and D. Carpentier, "Topological weyl semi-metal from a lattice model," EPL **97**, 67004 (2012).

[36] B. Singh, A. Sharma, H. Lin, M.Z. Hasan, R. Prasad, and A. Bansil, "Topological electronic structure and Weyl semimetal in the $TlBiSe_2$ class of semiconductors," Phys. Rev. B **86**,

115208 (2012).

[37] C. Fang, M. J. Gilbert, X. Dai, and B. A. Bernevig, "Multi-Weyl topological semimetals stabilized by point group symmetry," Phys. Rev. Lett. **108**, 266802 (2012).

[38] L. Lu, L. Fu, J.D. Joannopoulos, and M. Soljacic, "Weyl points and line nodes in gyroid photonic crystals," Nat. Photonics **7**, 294–299 (2013).

[39] L. Lu, J. D. Joannopoulos, and M. Soljacic, "Topological photonics," Nat. Photonics **8**, 821–829 (2014).

[40] J. Liu and D. Vanderbilt, "Weyl semimetals from noncentrosymmetric topological insulators," Phys. Rev. B **90**, 155316 (2014).

[41] D. Bulmash, C.-X. Liu, and X.-L. Qi, "Prediction of a Weyl semimetal in $Hg_{1-xy}Cd_xMn_yTe$," Phys. Rev. B **89**, 081106 (2014).

[42] S.-M. Huang, S.-Y. Xu, I. Belopolski, C.-C. Lee, G. Chang, B. Wang, N. Alidoust, G. Bian, M. Neupane, C. Zhang, S. Jia, A. Bansil, H. Lin, and M. Z. Hasan, "A Weyl fermion semimetal with surface fermi arcs in the transition metal monopnictide TaAs class," Nat. Comm. **6**, 7373 (2015).

[43] H. Weng, C. Fang, Z. Fang, B. A. Bernevig, and X. Dai, "Weyl semimetal phase in noncentrosymmetric transition-metal monophosphides," Phys. Rev. X **5**, 011029 (2015).

[44] T. Dubcek, C. J. Kennedy, L. Lu, W. Ketterle, M. Soljacic, and H. Buljan, "Weyl points in three-dimensional optical lattices," Phys. Rev. Lett. **114**, 225301 (2015).

[45] L. Lu, Z. Wang, D. Ye, L. Ran, L. Fu, J.D. Joannopoulos, and M. Soljacic, "Experimental observation of Weyl points," Science **349**, 622–624 (2015).

[46] S.-Y. Xu, I. Belopolski, N. Alidoust, M. Neupane, C. Zhang, R. Sankar, S.-M. Huang, C.-C. Lee, G. Chang, B. Wang, G. Bian, H. Zheng, D. S. Sanchez, F. Chou, H. Lin, S. Jia, and M. Zahid Hasan, "Experimental realization of a topological Weyl semimetal phase with Fermi arc surface states in TaAs," Science **349**, 613–617 (2015).

[47] B. Q. Lv, H. M. Weng, B. B. Fu, X. P. Wang, H. Miao, J. Ma, P. Richard, X. C. Huang, L. X. Zhao, G. F. Chen, Z. Fang, X. Dai, T. Qian, and H. Ding, "Discovery of Weyl semimetal TaAs," (2015), arXiv:1502.04684.

[48] S. G. Johnson and J. D. Joannopoulos, "Three-dimensionally periodic dielectric layered structure with omnidirectional photonic band gap," Appl. Phys. Lett. **77**, 34903492 (2000).

[49] M. Qi, E. Lidorikis, P. T. Rakich, S. G. Johnson, J. D. Joannopoulos, E. P. Ippen, and H. I.

Smith, "A three-dimensional optical photonic crystal with designed point defects," Nature **429**, 538–542 (2004).

[50] M. L. Povinelli, Steven G. Johnson, Shanhui Fan, and J. D. Joannopoulos, "Emulation of two-dimensional photonic crystal defect modes in a photonic crystal with a three-dimensional photonic band gap," Phys. Rev. B **64**, 075313 (2001).

[51] E. Lidorikis, M. L. Povinelli, S. G. Johnson, and J. D. Joannopoulos, "Polarization-independent linear waveguides in 3D photonic crystals," Phys. Rev. Lett. **91**, 023902 (2003).

[52] S. G. Johnson and J. D. Joannopoulos, "Block-iterative frequency-domain methods for Maxwell's equations in a planewave basis," Opt. Express **8**, 173–190 (2001).

[53] S. Kageyama, M. Akagawa, and H. Fujiwara, "Dielectric function of *a*-Si:H based on local network structures," Phys. Rev. B **83**, 195205 (2011).

[54] E. D. Palik (Ed.), *Handbook of Optical Constant in Solids, Vol. 2* (Academic Press, 1997).

[55] A. K. Geim and I. V. Grigorieva, "Van der Waals heterostructures," Nature **499**, 419–425 (2013).